

InP-based Geiger-mode avalanche photodiode arrays for three-dimensional imaging at 1.06 μm

Mark A. Itzler*, Mark Entwistle, Mark Owens, Xudong Jiang, Ketan Patel, Krystyna Slomkowski, Tim Koch, and Sabbir Rangwala

Princeton Lightwave Inc., 2555 US Route 130 South, Cranbury, NJ 08512

Peter F. Zalud, Young Yu, John Tower, and Joseph Ferraro
Sarnoff Corp., 201 Washington Road, Princeton, NJ 08543

ABSTRACT

We report on the development of 32 x 32 focal plane arrays (FPAs) based on InGaAsP/InP Geiger-mode avalanche photodiodes (GmAPDs) designed for use in three-dimensional (3-D) laser radar imaging systems at 1064 nm. To our knowledge, this is the first realization of FPAs for 3-D imaging that employ a planar-passivated buried-junction InP-based GmAPD device platform. This development also included the design and fabrication of custom readout integrate circuits (ROICs) to perform avalanche detection and time-of-flight measurements on a per-pixel basis. We demonstrate photodiode arrays (PDAs) with a very narrow breakdown voltage distribution width of 0.34 V, corresponding to a breakdown voltage total variation of less than +/- 0.2%. At an excess bias voltage of 3.3 V, which provides 40% pixel-level single photon detection efficiency, we achieve average dark count rates of 2 kHz at an operating temperature of 248 K. We present the characterization of optical crosstalk induced by hot carrier luminescence during avalanche events, where we show that the worst-case crosstalk probability per pixel, which occurs for nearest neighbors, has a value of less than 1.6% and exhibits anisotropy due to isolation trench etch geometry. To demonstrate the FPA response to optical density variations, we show a simple image of a broadened optical beam.

Keywords: avalanche photodiodes, single photon detector, photon counting, Geiger-mode APD, lidar, three-dimensional imaging, InP, InGaAsP

1. INTRODUCTION

The ability to image scenes and objects in three dimensions (i.e., angle-angle-range) provides tremendous advantages relative to other imaging techniques. By employing high-resolution range measurements at each pixel of the imager, the user can obtain image data in three spatial dimensions that allows for robust target recognition that is superior to the use of traditional two-dimensional intensity images. Intensity images require that object shapes be inferred from edge examination and complex image processing algorithms that generally require assumptions about the object or scene that are not implicit in the image data. Three dimensional data removes the ambiguity of edge determination and provides far more definitive information concerning imaged targets.

Three-dimensional imaging [1,2] enables the acquisition of data that is generally not possible using two-dimensional imaging technology, including the imaging of targets behind camouflage netting and obscuring foliage or tree canopy. The 3-D technique works by exploiting randomly positioned voids in netting or foliage that expose image targets that are otherwise veiled by these obscuring foreground elements. As the sensor platform moves, a new distribution of voids reveals additional information pertaining to the targets. Fusion of multiple image frames allows for a high-resolution 3-D image of the target to be formed. The use of short laser pulses of a few ns duration provides much higher resolution imaging than longer wavelength sensing techniques (e.g., radar) and results in far more successful target identification and recognition. The extension of the 3-D imaging concept to detectors with single photon sensitivity [3] provides unparalleled sensitivity, with greatly relaxed requirements on the launched power of optical pulses.

This work was sponsored by the Defense Advanced Research Projects Agency under contract HR0011-08-C-0021. Approved for Public Release, Distribution Unlimited.

*mitzler@princetonlightwave.com; tel: 1 609 495 2551; www.princetonlightwave.com

Foreground camouflaging elements can be readily removed using the explicit depth information obtained by each pixel of the single-photon 3-D imager. The problem of blinding by early-returning photons (reflected by the camouflaging foreground) can be avoided by working with sufficiently low power laser pulses so that the probability of receiving more than one photon per pixel per image frame is small. Even if very few photons reflect off of the target of interest and successfully reach the 3-D imager by traversing the camouflage in two passes, the ability to measure single photons provides image data and constitutes the most efficient use of transmitter power. By accumulating multiple frames of data at high repetition rates using low power pulses, one obtains the maximum information extraction from each photon along with good statistics for image construction based on intensity as well as range.

In this paper, we report on the development of focal plane arrays (FPAs) for 3-D imaging systems with single photon sensitivity employing two-dimensional arrays of InGaAsP-based Geiger-mode avalanche photodiodes (GmAPDs) with high-efficiency single photon sensitivity at 1.06 μm . In designing the GmAPD arrays, we have used a planar-passivated avalanche photodiode device platform with buried p-n junctions that has demonstrated excellent performance uniformity, operational stability, and long-term reliability. For 32 x 32 GmAPD arrays, we describe array-level data for which all 1024 detectors exhibit breakdown voltages within a total distribution width of 0.34 V, corresponding to a breakdown voltage variation of less than $\pm 0.2\%$. We describe FPA-level characterization as a function of excess bias and operating temperature following the hybridization of GmAPD arrays to CMOS read-out integrated circuits (ROICs). At an array-level excess bias voltage of 3.3 V, which provides 40% photon detection efficiency, we find average dark count rates of 2 kHz and a dark count rate standard deviation of less than 1 kHz for an operating temperature of 248 K. We also present detailed analysis of the optical crosstalk between pixels originating from hot carrier luminescence that occurs during avalanche events.

2. DESIGN OF FPA COMPONENTS AND MODULE

The GmAPD FPA module described in this paper is comprised of a number of critical components, including a photodiode array (PDA), a readout integrated circuit (ROIC), an interposer board, a thermoelectric cooler (TEC) and temperature sensor, and other packaging materials. Fully assembled modules also include a GaP microlens array to ensure high collection efficiency at each pixel, although we defer further description of modules with microlens arrays to a later publication. In this section, we discuss the design of the PDA, the ROIC, and overall module construction.

2.1 Geiger-mode avalanche photodiode (GmAPD) arrays

When an avalanche photodetector is biased above its breakdown voltage V_b , the creation of a single electrical carrier can induce a run-away avalanche that gives rise to a detectable macroscopic current. In this mode of operation, often referred to as Geiger mode, the detector is sensitive to the absorption of a single photon. (For this reason, these detectors are also often referred to as single photon avalanche diodes, or SPADs.) Our 1.06 μm GmAPD device design shares similarities with InP/InGaAs GmAPD designs we have employed for longer wavelength operation with a 1.67 μm room-temperature cutoff [4]. We have described in detail the design, simulation, and characterization of discrete GmAPD devices employing both InGaAs and InGaAsP absorption regions in previous publications. [4 – 9]

To enable FPA sensors based on GmAPD devices, we have fabricated a first generation of detector arrays in a 32 x 32 format with 100 μm pixel pitch. A schematic depiction of the GmAPD device structure is illustrated in Figure 1. Photon absorption occurs in a quaternary InGaAsP layer ($E_g \sim 1.03$ eV), lattice-matched to InP and optimized for detection at 1.06 μm at operating temperatures in the range from $\sim 240 - 260$ K. This absorption layer is spatially separated from a wider bandgap InP region ($E_g \sim 1.35$ eV) in which avalanche multiplication occurs. A primary goal of the design — the separate absorption and multiplication (SAM) region structure [10] — is to maintain low electric field in the narrower bandgap absorber (to avoid dark carriers due to tunneling) while maintaining sufficiently high electric field in the multiplication region (so that impact ionization leads to significant avalanche multiplication). The inclusion of a charged layer between the absorption and multiplication regions (the SACM structure [11]) allows for more flexible tailoring of the internal electric field profile, along with the associated avalanche process, and is common to many InP-based avalanche diodes used today. Grading layers between the InGaAsP and InP layers are added to mitigate carrier (specifically hole) trapping effects that result from the valence band offset that arises in an abrupt heterojunction of InGaAsP and InP [12].

The creation of a single electron-hole pair by photoexcitation in the InGaAsP layer results in the injection of the hole into the high-field InP multiplication region in which impact ionization results in avalanche gain. With the GmAPD biased above V_b in its armed state, the resulting avalanche gives rise to a macroscopic current pulse that is sufficiently large to be sensed by a threshold detection circuit contained in the readout integrated circuit, described below. Unlike linear mode APDs operated below V_b , the GmAPD detection process is inherently digital, and with appropriately designed detectors and threshold circuits, the detection process is noiseless.

The lateral structure of our design employs a buried p-n junction to guarantee edge breakdown suppression, low perimeter leakage, and high reliability. The device active area geometry is determined by the patterning of a SiN dielectric passivation layer to create a diffusion mask. A subsequent diffusion of Zn dopant atoms creates a p^+ -InP region within the i-InP cap layer. The quasi-cylindrical junction that is formed by a single diffusion exhibits electric field enhancement where the junction curvature is maximum and leads to premature avalanche breakdown at the edges of the device. To suppress this edge breakdown phenomenon, we use two diffusions to tailor the junction profile [13] so that the junction is deeper in the central part of the active area than it is in the junction periphery. This design ensures that the gain profile across the center part of the active region is uniform and that the gain is reduced in the peripheral region of the device. For the arrays described in this paper, the optical active region diameter in each pixel was $34\ \mu\text{m}$. With this buried junction design, the formation of a high-quality SiN passivation layer can guarantee low perimeter leakage and stable long-life performance.

To investigate crosstalk effects in arrays of planar-geometry GmAPDs, we have fabricated structures containing etched isolation trenches between pixels (as shown in Figure 1) as well as arrays without isolation trenches. The arrows in Figure 1 illustrate two dominant paths by which photons emitted by hot carrier luminescence during an avalanche event in one pixel can couple to the active region of a neighboring pixel and induce correlated crosstalk events. We have found that in our planar-geometry arrays, the coupling along the direct “line-of-sight” path can be significantly attenuated by introducing etched trenches between the pixel active areas. Coupling to pixels beyond the nearest neighbors is dominated by reflections from the back surface of the GmAPD die.

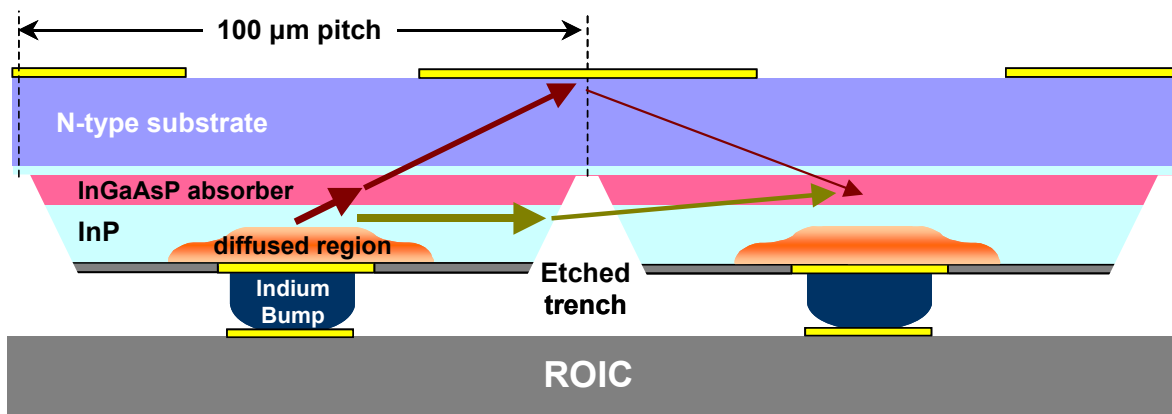


Figure 1. Schematic representation of $1.06\ \mu\text{m}$ planar-geometry diffused-junction GmAPD focal plane array. The photodiode array (PDA) is bump-bonded to a silicon CMOS readout integrated circuit (ROIC). Arrows indicate two dominant paths for optical crosstalk caused by avalanche carrier luminescence involving (i) direct line-of-sight coupling through etched trenches or (ii) back-reflections from the rear surface of the PDA chip.

Arrays of related mesa-geometry InP-based GmAPD have been extensively studied in pioneering work by researchers at MIT-Lincoln Laboratory [14 – 16], and significant additional work on mesa-geometry devices has also been recently reported. [17,18]. These devices are based on an epitaxial structure similar to that used for our planar geometry devices. However, instead of using dopant diffusions to define the active region p-n junctions, their p-n junctions are epitaxially grown, and their active areas are defined by the etching of mesas in which all epi-grown material is removed outside the intended active region. To control edge breakdown effects in mesa-geometry devices, the GmAPD structure is grown on p-type InP substrates and has a dopant polarity opposite to that of our planar-geometry devices.

The GmAPD array fabrication includes back-side anti-reflection-coated apertures aligned to the pixel active regions as well as front-side patterning of indium bumps to facilitate hybridization of the detectors to a mating 32 x 32 CMOS ROIC, which is described briefly in the next sub-section.

2.2 CMOS readout integrated circuits (ROICs)

The CMOS ROIC performs several critical functions in the operation of the GmAPD FPA. In the disarmed state, every pixel in the detector array is biased slightly below the breakdown voltage of the GmAPD. Each frame begins with the arming of all of the detector pixels by applying an excess bias, generally up to 5 V. The period during which the pixels remained armed is the range gate — typically on the order of a few microseconds — and the beginning of the range gate is synchronized (perhaps up to a fixed delay) with the launch of an optical pulse from which reflected photons will be detected. Within each ROIC pixel, there is a threshold detection circuit that triggers when an avalanche event occurs in the corresponding armed pixel of the photodiode array. When this trigger occurs, an active quenching circuit removes the excess bias from the fired GmAPD pixel to disarm it, and an in-pixel counter is stopped so that the time of detection within the range gate is recorded. At the end of each range gate, pixels that do not sense an avalanche event record the terminal counter value, indicating that no event has occurred. The frame readout then consists of scanning out all of the pixel counter values. This FPA architecture provides range resolution corresponding to the timing resolution of the pixel counters, whereas the intensity resolution is one bit per frame. Intensity information within the 3-D image data is obtained by accumulating multiple frames.

In the work described below, we have developed FPAs using two different ROICs. The first is a circuit developed by MIT Lincoln Laboratory (MIT-LL) that has been described previously [3,16]. This ROIC employs 10-bit counters within each pixel with a pseudo-random counter design that occupies a relatively small area compared with other counter designs. The clock signal provided by an on-chip ring oscillator is used to create two additional vernier bits (using a copy of the clock with a 90 degree phase shift) to provide 12-bit counter data. Pixel counter data is scanned out using 16 input/output ports on which data from each pair of adjacent rows is interleaved. Due to board design limitations, we were constrained to frame rates on the order of 5 kHz.

The second ROIC we employed was a custom circuit designed by the authors specifically for this FPA development effort. We selected a pseudo-random counter architecture similar to the MIT-LL counter design that also employed the 2-bit vernier scheme, but we increased the counter resolution to 11 bits, for an overall timing resolution of 13 bits. The data scan out design provided for a dedicated I/O port for each of the 32 rows in the array, and high-speed scan out circuitry allows for frames rates exceeding 200 kHz. For typical frame rates on the order of 20 kHz, the power dissipation of this custom ROIC was found to be less than 40 mW.

2.3 FPA module design

The GmAPD photodiode array and CMOS ROIC are hybridized using flip-chip bonding with indium bumps. This chip stack is then bonded to a ceramic interposer that provides for electrical routing of all signals to and from the ROIC. The interposer is assembled onto a two-stage thermoelectric cooler within a ceramic package that also provides pin-grid array electrical feedthroughs. A CuW heatsink allows for thermal grounding of the module, which allows for cooling of the GmAPD detector arrays to a temperature at least as low as 240 K. Various lid configurations have been used to seal the package and provide optical access to the sensor. A solid body cut-away schematic in Figure 2(a) illustrates the overall module assembly design, and the photograph in Figure 2(b) exhibits an assembled module (without lid) employing a chip stack that includes our custom ROIC.

3. PHOTODIODE WAFER-LEVEL CHARACTERIZATION

Prior to dicing wafers into singulated GmAPD die, we performed array-level characterization entailing fixed-point current-voltage (I-V) characteristics for all 1024 detectors on 32 x 32 arrays. The most critical device I-V characteristic is the avalanche breakdown voltage V_b of each pixel, which we define to be the voltage at which the dark current reaches 10 μ A. Single photon detection parameters such as dark count rate, detection efficiency, and crosstalk increase monotonically with excess bias V_{ex} , where V_{ex} is defined to be the voltage increment by which the applied voltage V_a exceeds V_b — i.e., $V_{ex} = V_a - V_b$. Therefore, to achieve highly uniform photon detection characteristics across the array, it is necessary to have the distribution of V_b across the array be as uniform as possible. Moreover, with all existing

ROIC designs for GmAPD FPAs, a single bad detector pixel with excessively large leakage can render the entire FPA unusable. The existence of low V_b pixels will generally lead to excessively high leakage at the mean V_b level is applied to the rest of the array. Therefore, sufficiently uniform V_b is critical from the perspective of fundamental FPA yield considerations.

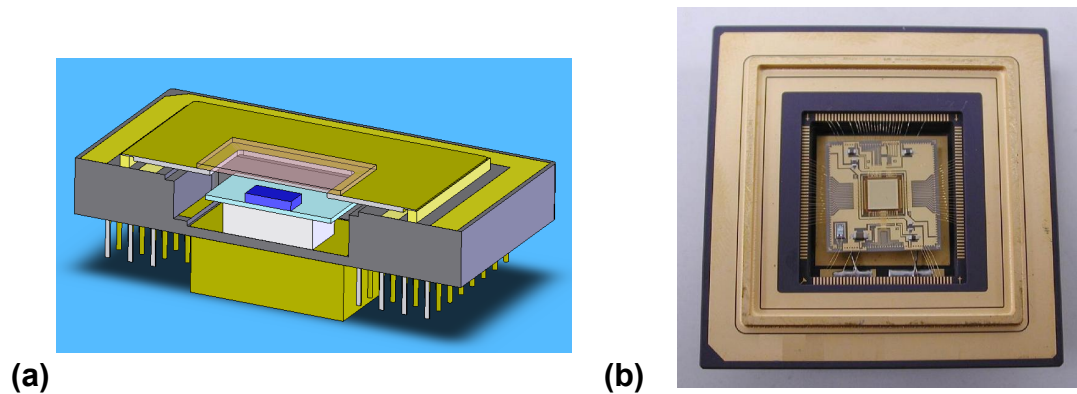


Figure 2. (a) Solid body model of FPA prototype module with cut-away showing, from bottom to top, CuW heatsink (gold), ceramic package (gray), thermoelectric cooler (white), interposer with electrical routing (light blue), hybridized PDA+ROIC chip stack (dark blue), and package window (clear). (b) Photograph of assembled prototype module (without lid).

In Figure 3, we present data obtained from array-level probing for the breakdown voltage of all elements of a sample 32×32 array. The histogram in Figure 3(a), which contains V_b data from all 1024 elements, demonstrates that the entire distribution width is 0.35 V with no outliers. The standard deviation of this distribution is 0.056 V and represents a variation of less than 0.1% relative to the mean breakdown voltage of ~ 85.1 V.

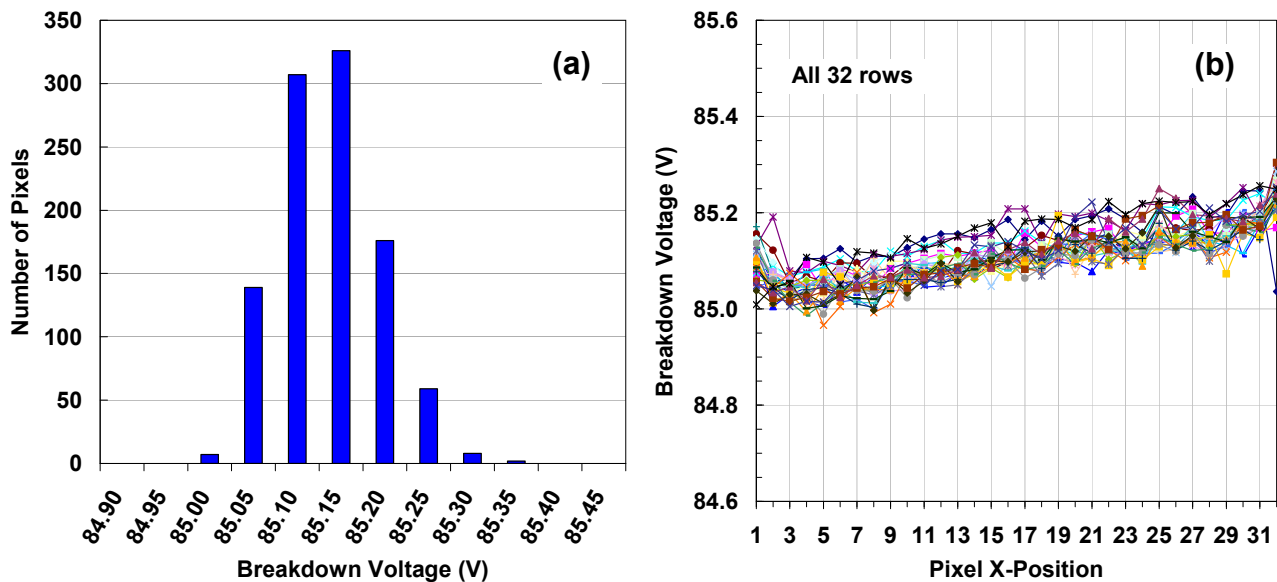


Figure 3. Pixel-level data for the breakdown voltage for all 1024 pixels of a 32×32 GmAPD photodiode array. (a) Histogram of breakdown voltages for all 1024 pixels with a standard deviation of 0.056 V and a total range of 0.35 V with no outliers. (b) Breakdown voltage data as a function of pixel X-position for all 32 rows in the 32×32 array.

The spatial variation in V_b is exhibited in Figure 3(b), in which we have plotted V_b along all 32 rows of the array as a function of the X-position along each row. These data show that the total range of variation in V_b along any given X-position is less than 0.15 V, but there is a systematic variation in the mean V_b for higher X-position rows. This systematic variation in V_b is due to spatial variations in the GmAPD epitaxial structure, with the most critical design

elements being the width of the avalanche region (between the diffused region and the InGaAsP absorber – see Figure 1) and the charge layer used to control the electric field in the avalanche region (e.g., see [4]). The degree of structural variation will depend on the precise position of the GmAPD array chip on the wafer, but the change of ~0.15 V over the 3.2 mm dimension of the array is about the largest variation seen. (Variations are radial and correspond to ~1 V variation over a 25 mm wafer radius.)

4. RESULTS FOR DARK COUNT RATE AND PHOTON DETECTION EFFICIENCY

The two most fundamental performance parameters for single photon detectors are the photon detection efficiency (PDE) and the dark count rate (DCR). The PDE is the probability that the arrival of a photon at the detector gives rise to a detection event, whereas the DCR is the probability that a detection event occurs in the absence of a photon arrival. The PDE is actually the product of three probabilities: $PDE = \eta P_c P_a$, where η is the quantum efficiency of the absorption layer, P_c is the probability that photoexcited carriers are collected by injection into the avalanche region, and P_a is the probability that a carrier injected into the avalanche region gives rise to a detectable avalanche. Note that P_a is in part determined by the details of the threshold detection circuit that follows the detector.

The DCR is determined by mechanisms other than photoexcitation that give rise to carriers which can trigger avalanche events. In a well-designed GmAPD, the DCR generally consists of two principal contributions: thermal excitation of carriers in the narrow bandgap absorber layer, which dominates for higher temperature operation; and carrier tunneling effects in the high-field avalanche multiplication region, which dominate for lower temperature operation. We have reported details concerning simulations of PDE and DCR in earlier publications [5 – 7] in which we adopted a modeling formalism initially developed by researchers at MIT-LL [15,16].

4.1 DCR vs. PDE for discrete test devices and comparison to modeling

In the fabrication of GmAPD array wafers, discrete GmAPD test devices have been included to allow for device characterization using existing measurement apparatus that has been benchmarked through the testing of a large quantity of discrete production GmAPDs that Princeton Lightwave has been selling for the past several years. Figure 4 shows characterization results for DCR vs. excess bias for five test devices with 34 μm active areas (as used in our default GmAPD array design) at an operating temperature of 240 K. Also plotted with the experimental data is the simulation for DCR vs. excess bias given our GmAPD design structure, which shows good agreement with the measured data.

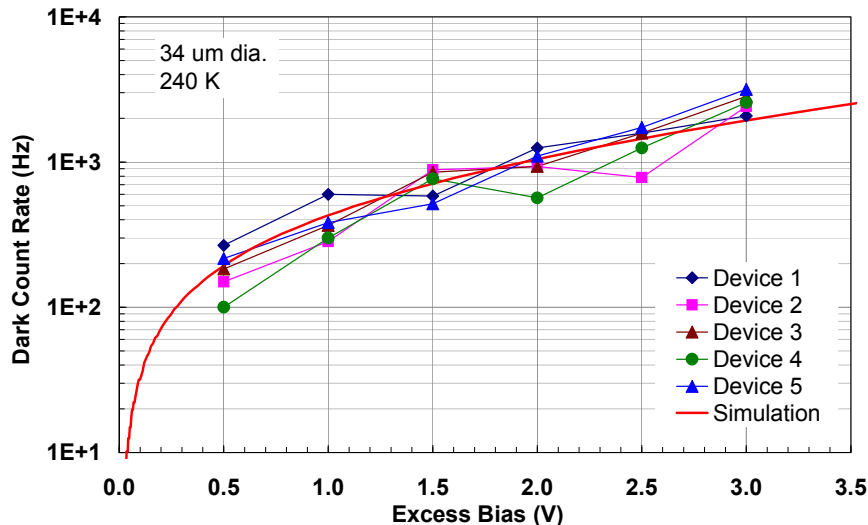


Figure 4. Characterization results for dark count rate vs. excess bias at 240 K for five discrete test devices with 34 μm active areas fabricated along with GmAPD arrays. The solid curve without symbols indicates the output of simulations for our GmAPD device design.

4.2 FPA-level characterization of DCR and PDE

To perform comprehensive characterization of the FPAs, we developed FPGA-based electronics interface boards for managing all I/O and control signals, including high-speed data readout for storage on a desktop computer via a 32 channel data acquisition card. Custom software allows the user to specify all operating conditions, including range gate length, number of frames to be collected, excess bias to be applied, and the subset of the FPA pixels from which to collect data (from single pixel to the entire 32 x 32 array). To measure PDE, we implemented a three-axis translation system to position the focused output of an optical fiber with micron-scale precision. When optimally focused, this set-up provided a spot size of about 8 μm width. This allowed us to accurately scan the effective width of the pixel active area and confirm its consistency with the designed value of 34 μm .

Initial FPA characterization consisted of the measurement of PDE at the single-pixel level as well DCR, for which averaging over a large number of pixels could be readily performed. The data in Figure 5(a) illustrate the dependence of both DCR and PDE on excess bias at an operating temperature of 248 K. The DCR was obtained from averaging over a 16 x 16 pixel area of the FPA for 10,000 frames of data. The PDE was also obtained using 10,000 frames of data, but for a single pixel. The PDE data shown were typical of numerous different pixels measured. Given that the trade-off between DCR and PDE is critical in GmAPD operation, it is most useful to plot DCR vs. PDE using data pairs obtained at the same excess bias. Using the data from Figure 5(a), we plot the corresponding behavior of DCR vs. PDE in Figure 5(b). For an operating temperature of 248 K, a low DCR value of 2 kHz is obtained for a PDE of 40%, and PDE values up to 48% were measured with DCR remaining below 10 kHz

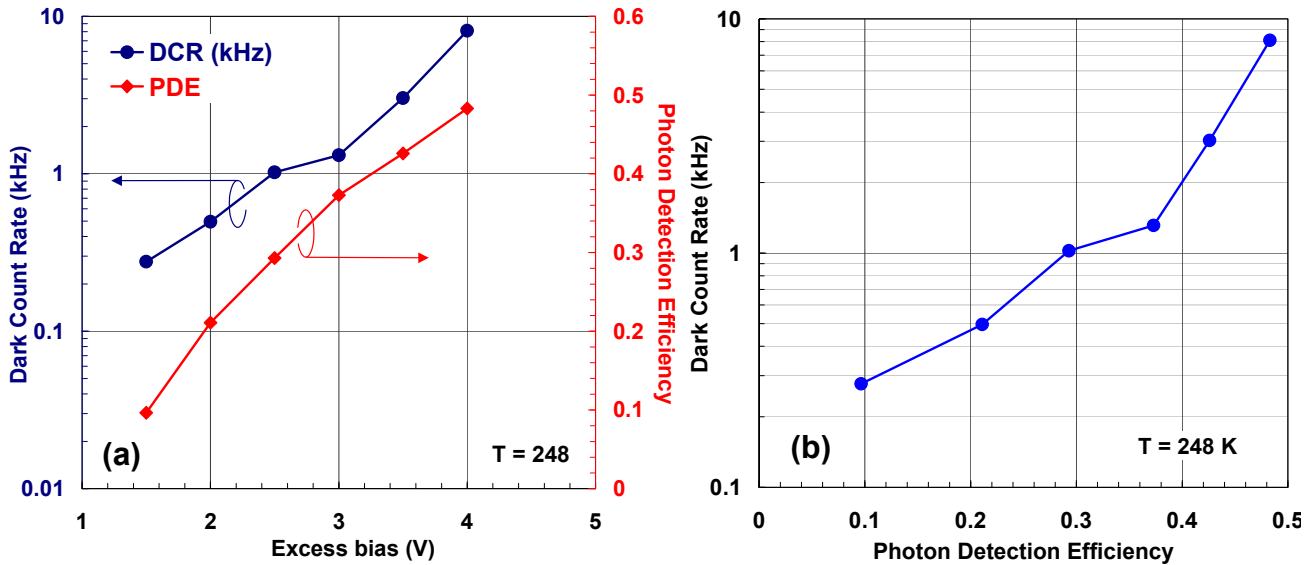


Figure 5. (a) Dark count rate (DCR) and photon detection efficiency (PDE) as a function of excess bias voltage obtained from a focal plane array operating at 248 K. DCR is the average of all pixels in a 16 x 16 area, and PDE is typical for single-pixel measurements. (b) Data from (a) plotted as DCR vs. PDE.

Whereas PDE remains relatively constant with changes in operating temperature, the DCR varies considerably due to the importance of dark carrier excitation by thermal generation mechanisms. As a rough rule of thumb, DCR will increase by about a factor of 2 for every 10 K increase in temperature, although the precise factor will depend on detailed conditions such as the excess bias and the starting temperature. The change in DCR vs. excess bias with temperature is demonstrated in Figure 6.

5. CHARACTERIZATION AND ANALYSIS OF OPTICAL CROSSTALK

A potential limitation in the performance of GmAPD-based FPAs is the optical crosstalk that can occur when hot carrier luminescence results from avalanche events. The acceleration of charge in the high-field avalanche region causes photon emission at the rate of one photon per $10^5 - 10^6$ carriers that flow through the avalanche region. Because all

pixels are sensitive to single photons, the coupling of emitted photons to neighboring active areas can cause correlated spurious crosstalk avalanche events at these neighbors. We illustrated the two primary optical crosstalk paths in Figure 1, where the direct “line-of-sight” path couples emitted photons to nearest neighbor absorption regions, while back-reflections from the rear surface of the GmAPD chip can couple photons to further neighbors. In this section, we describe our analysis of FPA-level data to extract crosstalk performance.

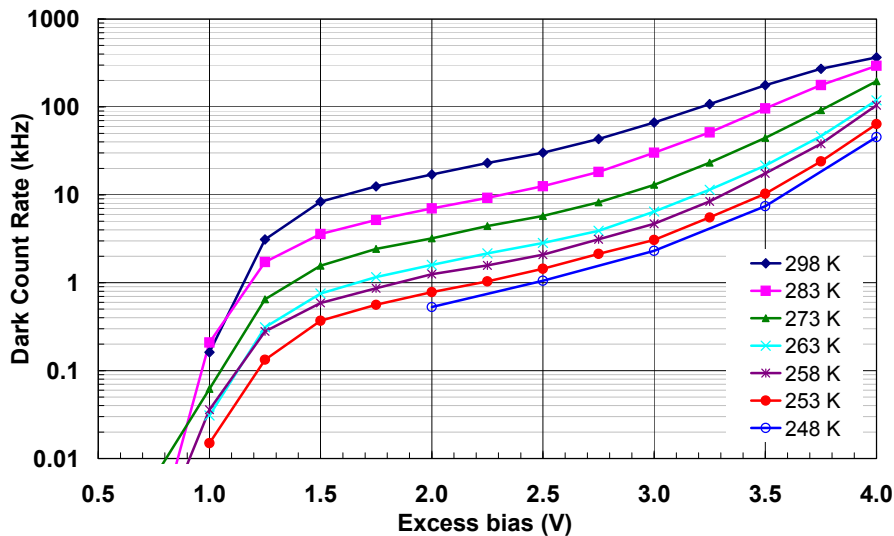


Figure 6. Dark count rate as a function of excess bias voltage, at temperatures varying from 248 K to 298 K, obtained from the average of a typical 16 x 16 region of a focal plane array.

5.1 Dependence of crosstalk on spatial separation between pixels

We extracted FPA-level crosstalk performance from count data obtained solely from dark counts as well as using count data obtained using single pixel illumination. In both cases, we used the same analysis. Because we have timing data for all avalanche events, we can search for temporal correlations as well as spatial correlations. We begin by scanning the data for a “trigger” pixel that experienced an avalanche event, as evidenced by a counter value less than the terminal count for the range gate used. We then search for all pixels that may have fired at nearly the same time as the “trigger” pixel. To choose an appropriate time window, we analyzed the temporal correlation of assumed crosstalk counts with test “trigger” pixels and determined that correlations decayed to the background DCR level for delays of greater than 10 ns. Therefore, we assume that any avalanche event within 10 ns of the “trigger” avalanche is correlated.

To obtain crosstalk data from DCR measurements, we stored 1000 frames of DCR data from the entire 32 x 32 FPA and searched each frame for “trigger” events and any neighboring events occurring within 10 ns of the “trigger”. From this analysis, we compiled the probability of a crosstalk event as a function of the distance between the “trigger” pixel and the crosstalk pixel. The average crosstalk probability per pixel for DCR data is plotted in Figure 7 as a function of the distance between pixel centers, where the unit of distance is assumed to be the pixel pitch of 100 μm . Distance values of 1 correspond to nearest neighbors in the horizontal and vertical directions, values of ~ 1.4 correspond to diagonal neighbors, and so on. Crosstalk data are presented for five different excess bias values spanning the range from 1.5 V to 3.5 V, and it is clear that crosstalk increases dramatically for larger excess bias. Additionally, while the data show a decrease in crosstalk with increasing interpixel distance D that could be consistent with an expected $1/D^2$ rolloff, there is non-monotonic behavior that depends quite sensitively on the precise location of a particular crosstalk pixel.

For avalanche events induced by intentional single photon illumination at a specific “trigger” pixel, we can apply the same analysis as used for the DCR data, although we can restrict our search to a much narrower range of pixels surrounding the illuminated pixel. In Figure 7(b), we present the crosstalk probability per pixel as function of the distance between pixels for the case of an illuminated “trigger” pixel. We again used 1000 frames of data, but sufficient data were obtained by using only a 9 x 9 region of pixels with the illuminated pixel at its center. The overall trend in

the crosstalk behavior extracted from the illuminated pixel case is very similar to behavior seen in Figure 7(a) for the dark count triggers, especially for the higher excess bias values for which crosstalk amplitudes are larger and therefore less subject to noise in the data.

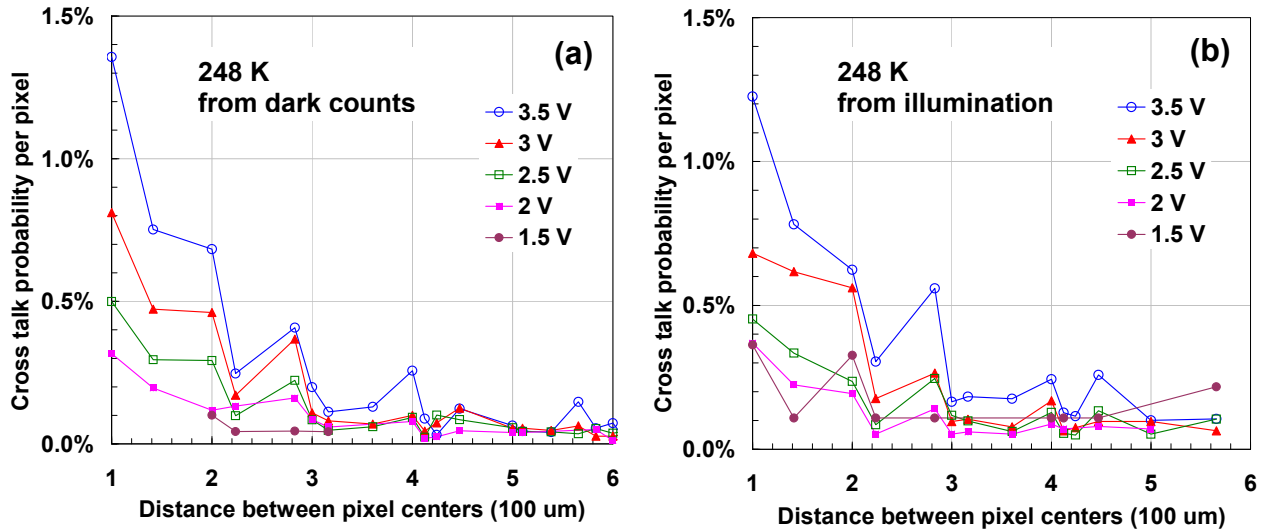


Figure 7. Dependence of cross talk probability per pixel on distance between pixel centers for five different values of excess bias between 1.5 V and 3.5 V. Cross talk is identified by considering an initial count at one pixel and determining whether any nearby pixels fired within 10 ns of the initial count. In (a), DCR data is analyzed for such crosstalk correlations. In (b), a given pixel is illuminated with a single photon pulse to induce the initial count. Agreement between the two methods is very good.

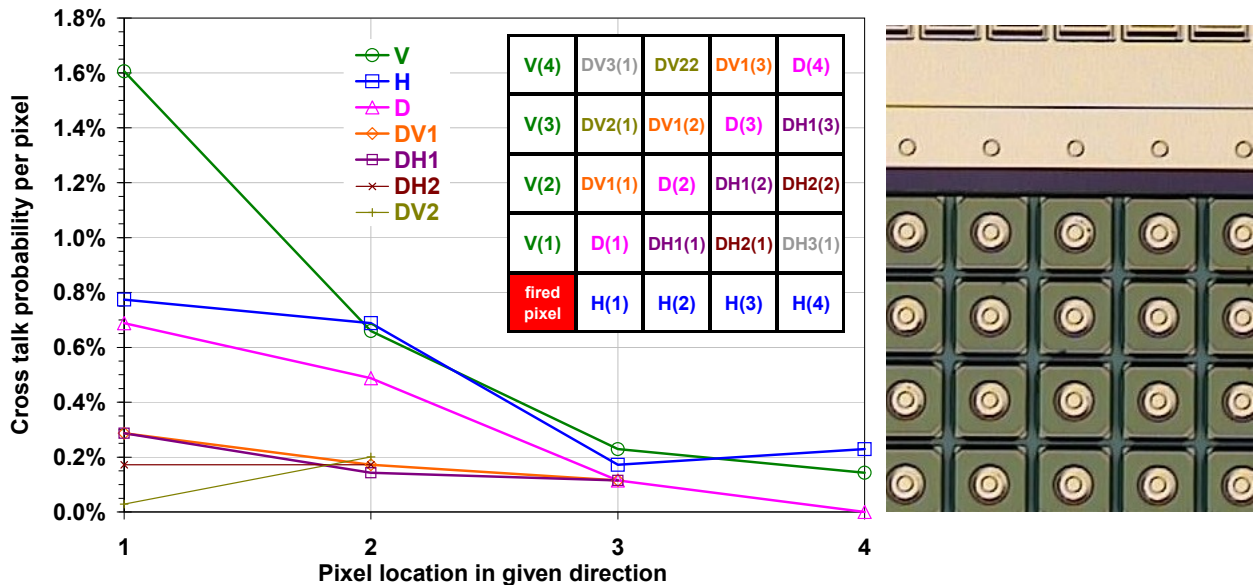


Figure 8. Dependence of crosstalk probability per pixel on pixel location indicates a strong crosstalk anisotropy for nearest neighbors in the vertical and horizontal directions. This near neighbor anisotropy results from anisotropy in the etching process used to create the trenches between active areas, as can be seen in the micrograph at right. Beyond the nearest neighbors, crosstalk data indicates essentially isotropic behavior.

5.2 Anisotropy effects in crosstalk behavior

A closer inspection of the crosstalk data described above reveals a difference in crosstalk amplitude per pixel for nearest neighbors in the horizontal and vertical directions. As illustrated in Figure 8, the crosstalk per pixel for the nearest neighbor pixel in the vertical direction (1.6%) is twice as large as for the nearest neighbor in the horizontal direction (0.8%). However, for next nearest neighbor pixels and beyond, the crosstalk in the vertical and horizontal directions is identical to within the accuracy of the measurements and subsequent analysis.

This crosstalk anisotropy originates from the geometric characteristics of the etched isolation trenches fabricated to reduce direct “line-of-sight” coupling between nearest neighbors. The micrograph at the right of Figure 8 illustrates a small portion of the array, and scanning electron microscope images confirm that the horizontal trenches have a V-groove geometry, while the trenches in the vertical direction have nominally straight walls with a slight dovetail at the base. These features are consistent with etch profiles expected from the etch chemistry used to create the trenches. The modeling of optical transmission through these features is complex and still in progress, but this behavior is extremely interesting from the perspective of gaining a better understanding of the line-of-sight coupling behavior. It is also worth noting that other variants of the GmAPD arrays without etched isolation trenches exhibited significantly higher crosstalk for nearest neighbors as well as further neighbors.

6. FPA-LEVEL OPTICAL PERFORMANCE

As a final example of FPA-level performance, we present a simple image of a divergent optical beam created by defocusing the optical spot used to measure single pixel PDE, as described above in sub-section 4.2. In Figure 9(a), we exhibit a color-coded count distribution showing optical intensity across half of the FPA (i.e., a 32 x 16 pixel area) obtained by capturing 10,000 frames, in which each frame employed a 1 μ s range gate. The FPA was operated at 258 K with an excess bias corresponding to 40% PDE. The background DCR at these operating conditions is demonstrated for the same 32 x 16 pixel area in Figure 9(b) and has an average value of 3 kHz. The count values contained in each pixel are in kHz.

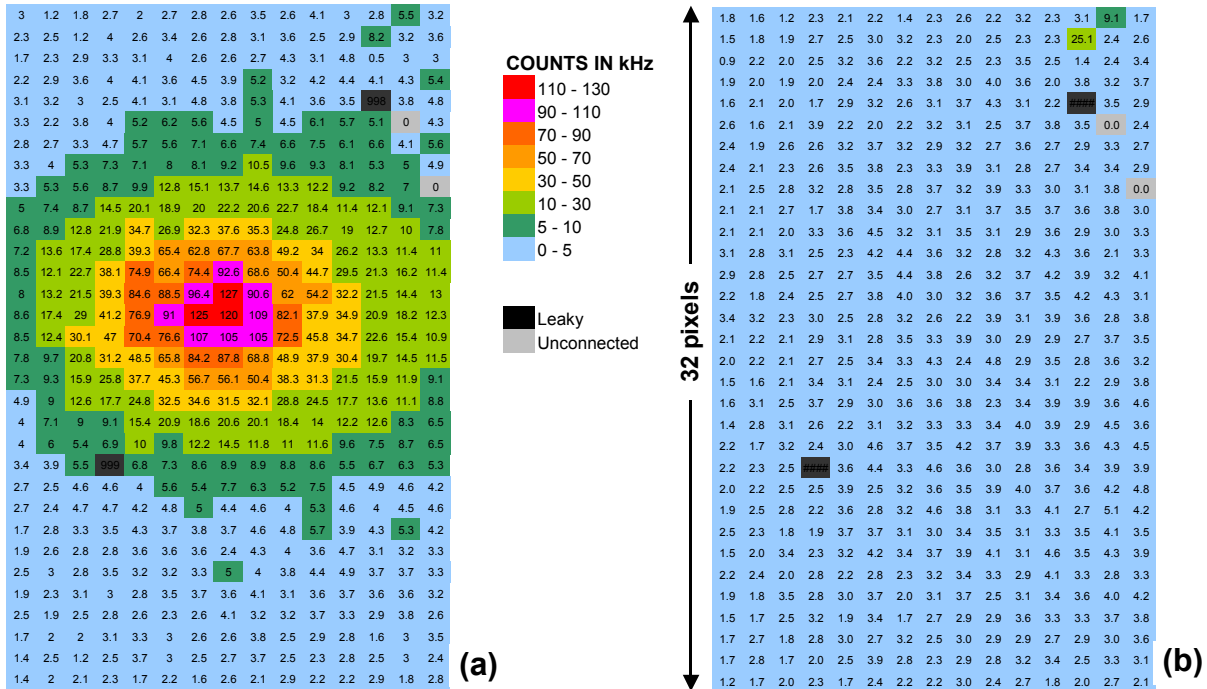


Figure 9. Count distribution of a 32 x 16 portion of an FPA exhibiting (a) the profile of a broad optical beam and (b) the background dark count distribution. Measurements were made at a PDE of 40% and a temperature of 258 K, for which the average pixel DCR was 3 kHz. The count values in each pixel are in kHz.

7. CONCLUSIONS

We have described the design and performance of 32 x 32 focal plane arrays with 100 μm pixel pitch based on InGaAsP Geiger-mode avalanche diodes in which time-of-flight measurements on a per-pixel basis allow for three-dimensional imaging with single photon sensitivity. In realizing these devices, we have implemented a planar-geometry GmAPD platform with planar passivation and buried p-n junctions fabricated using dopant diffusion. To our knowledge, this is the first report of GmAPD FPAs based on planar-geometry devices. We have also designed a custom readout integrated circuit that provides 13-bit timestamp data on a per-pixel basis with high frame rates exceeding 200 kHz. GmAPD arrays have been hybridized to ROICs by indium bump flip-chip bonding techniques, and the resulting chip stack has been assembled into a pin grid array package with an integrated two-stage thermoelectric cooler capable of providing operating temperatures at least as low as 240 K.

At operating temperatures on the order of 250 K, we have demonstrated dark count rates of 2 kHz at detection efficiencies of 40%. Extensive optical crosstalk characterization and analysis has been used to extract the dependence of crosstalk on the distance between pixels, and the worst-case crosstalk — which occurs for nearest neighbor pixels — is no larger than 1.6%. We have also demonstrated crosstalk anisotropy for nearest neighbors related to the geometry of etched trenches used to attenuate direct “line-of-sight” optical coupling. Finally, we demonstrated the ability of the FPA to measure optical density distributions by obtaining a simple image of a broadened optical beam.

ACKNOWLEDGMENTS

We are grateful to Dr. Monte Turner for his support throughout this work, for which we wish to acknowledge funding from DARPA. We also greatly appreciate the collaborative efforts of many colleagues at MIT Lincoln Laboratory, including Gary Smith, Alex McIntosh, Simon Verghese, Brian Aull, Brian Tyrrell, and Joe Funk.

REFERENCES

- [1] M. A. Albota, B. F. Aull, D. G. Fouche, *et al.*, “Three-dimensional imaging laser radars with Geiger-mode avalanche photodiode arrays,” *MIT Lincoln Laboratory Journal*, vol. 13, no. 2, p. 351 – 370 (2002).
- [2] B. F. Aull, A. H. Loomis, D. J. Young, *et al.*, “Three-dimensional imaging with arrays of Geiger-mode avalanche photodiodes,” *Proceedings of the SPIE* 5353, p. 105 – 116 (2004).
- [3] B. F. Aull, A. H. Loomis, D. J. Young, R. M. Heinrichs, B. J. Felton, P. J. Daniels, D. J. Landers, “Geiger-mode avalanche photodiodes for three-dimensional imaging,” *MIT Lincoln Laboratory Journal*, vol. 13, no. 2, p. 335 – 350 (2002).
- [4] M. A. Itzler, R. Ben-Michael, C.-F. Hsu, K. Slomkowski, A. Tosi, S. Cova, F. Zappa, and R. Ispasoiu, “Single photon avalanche diodes (SPADs) for 1.5 μm photon counting applications,” *J. Mod. Opt.*, vol. 54, no. 2-3, pp. 283-304 (2007).
- [5] M. A. Itzler, X. Jiang, R. Ben-Michael, K. Slomkowski, M. A. Krainak, S. Wu, and X. Sun, “InGaAsP avalanche photodetectors for non-gated 1.06 μm photon-counting receivers,” *Proceedings of the SPIE* 6572, 65720G (2007).
- [6] X. Jiang, M. A. Itzler, R. Ben-Michael, K. Slomkowski, “InGaAsP/InP Avalanche Photodiodes for Single Photon Detection,” *IEEE J. of Sel. Topics in Quantum Electronics* 13, p. 895 – 905 (2007).
- [7] X. Jiang, M. A. Itzler, R. Ben-Michael, K. Slomkowski, “InGaAsP avalanche photodetectors for near IR single photon detection,” *Proceedings of the SPIE* 6771, 677127 (2007).
- [8] X. Jiang, M. A. Itzler, R. Ben-Michael, K. Slomkowski, M. A. Krainak, S. Wu, and X. Sun, “Afterpulsing effects in free-running InGaAsP single photon avalanche diodes,” *IEEE J. Quantum Electron.*, vol. 44, p. 3 – 11 (2008).
- [9] M. A. Itzler, X. Jiang, R. Ben-Michael, B. Nyman, K. Slomkowski, “Single Photon Avalanche Diodes for Near-Infrared Photon Counting,” *Proceedings of the SPIE* 6900, 6900-48 (2008).
- [10] K. Nishida, K. Taguchi, and Y. Matsumoto, “InGaAsP heterostructure avalanche photodiodes with high avalanche gain,” *Appl. Phys. Lett.*, vol. 35, 251–252 (1979).
- [11] J. C. Campbell, A. G. Dentai, W. S. Holden, and B. L. Kasper, “High-performance avalanche photodiode with separate absorption, ‘grading’, and multiplication regions,” *Electron. Lett.*, vol. 19, 818 – 820 (1983).
- [12] S. R. Forrest, O. K. Kim, and R. G. Smith, “Optical response time of $\text{In}_{0.53}\text{Ga}_{0.47}\text{As}$ avalanche photodiodes,” *Appl. Phys. Lett.*, vol. 41, 95–98 (1982).
- [13] Y. Liu, S. R. Forrest, J. Hladky, M. J. Lange, G. H. Olsen, D. E. Ackley, *J. Lightwave Tech.*, vol. 10, 182 (1992).
- [14] K.A. McIntosh, J. P. Donnelly, D.C. Oakley, *et al.*, “InGaAsP/InP avalanche photodiodes for photon counting at 1.06 μm ,” *Appl. Phys. Lett.*, vol. 81 2505-2507 (2002).
- [15] J. P. Donnelly, E. K. Duerr, K. A. McIntosh, *et al.*, “Design Considerations for 1.06- μm InGaAsP-InP Geiger-Mode Avalanche Photodiodes,” *IEEE J. Quantum Electron.*, vol. 42, 797-809 (2006).

- [16] S. Verghese, J. P. Donnelly, E. K. Duerr, *et al.*, “Arrays of InP-based Avalanche Photodiodes for Photon Counting,” *IEEE Sel. Topics in Quantum Electron.* vol. 13, p. 870 – 886 (2007).
- [17] R. Sudharsanan, P. Yuan, J. Boisvert, P. McDonald, T. Isshiki, S. Mesropian, E. Labios, “Single photon counting Geiger mode InGaAs(P)/InP avalanche photodiode arrays for 3D imaging,” *Proceedings of the SPIE* 6950, 69500N (2008).
- [18] J. Boisvert, R. Sudharsanan, P. Yuan, T. Isshiki, P. McDonald, “Development of single photon counting sensors operating at short wavelength infrared wavelengths,” *Proceedings of the SPIE* 7222, 72221E (2009).